Deep Submarine Landslide Contribution to the 2010 Haiti Earthquake Tsunami

Adrien Poupardin[(1,2)], Eric Calais[(2)], Philippe Heinrich[(3)], Hélène Hébert[(3)], Mathieu Rodriguez[(2)], Sylvie Leroy[(4)], Hideo Aochi[(2,5)], and Roby Douilly [(6)]

5 [1]Institut de Recherche en Constructibilité, ESTP, Université Paris Est, Champ-sur-Marne, 77420, France
[2]Ecole normale supérieure, Dept. of Geosciences, PSL Research University, CNRS, Paris, 75005, France
[3]Commissariat à l'Energie Atomique, DAM, DIF, Arpajon, 91290, France
[4]Université Pierre et Marie Curie, Sorbonne Universités, CNRS, ISTeP, Paris, 75005, France
[5]Bureau de Recherches Géologiques et Minières, Orléans, 45000, France
10 [6]University of California, Riverside, Department of Earth Sciences, Riverside, 231, USA

Correspondence to: Adrien Poupardin (apoupardin@estp-paris.eu)

Abstract. The devastating M_w 7, 2010, Haiti earthquake was accompanied by local tsunamis that caused fatalities and damage to coastal infrastructure. Some were triggered by slope failures of river deltas in close vicinity of the epicenter, while others, 30 to 50 km to the north across the Bay of Gonâve, are well explained by the reverse component of coseismic ground motion

15 that accompanied this mostly strike-slip event. However, observations of run-up heights up to 2 m along the southern coast of the island at distances up to 100 km from the epicenter, as well as tide gauge and DART buoy records at distances up to 600 km from the epicenter have not yet received an explanation. Here we demonstrate that these observations require a secondary source, most likely a submarine landslide. We identify a landslide scar 30 km from the epicenter off the southern coast of Haiti at a depth of 3500 m, where ground acceleration would have been sufficient to trigger slope failure in soft sediments. This

20 candidate source, 2 km^3 in volume, matches observation remarkably well assuming that the sediment collapse obeys a viscous flow with an initial apparent viscosity of 2×10^5 Pa.s. Although that particular source cannot be proven to have been activated in 2010, our results add to a line of evidence that earthquake-triggered submarine landslides can cause significant tsunamis in areas of strike-slip tectonic regime.

1 Introduction

25 The devastating M_w 7, 2010, Haiti earthquake occurred within the Caribbean-North America plate boundary, where oblique relative motion at 19 mm/yr is partitioned between shortening on the North Hispaniola fault to the north and strike-slip motion on the E–W striking Septentrional and Enriquillo faults throughout the island (Fig. 1; Symithe et al., 2015). Although the earthquake was first assumed to have occurred on the Enriquillo fault, several independent studies later showed that it actually ruptured a previously unmapped fault – the Léogâne fault – with a source mechanism combining strike-slip and reverse faulting

30 (Calais et al., 2010; Hayes et al., 2010; Hashimoto et al., 2011; Symithe et al., 2013), in a setting resembling the 1989 Loma Prieta earthquake in California (e.g., Dietz and Ellsworth, 1990).

In spite of its moderate size and primarily strike-slip mechanism, the earthquake was accompanied by local tsunamis that caused at least three fatalities in Grand Goâve (Fritz et al., 2013) and some damage to coastal infrastructure. Thanks to the rapid deployment of an International Tsunami Survey Team (ITST), run-up height, flow depth, and inundation were
35 documented at more than 20 sites along Haitian coastline (Fig. 1; Fritz et al., 2013). Maximum tsunami heights reached 3 m in the close vicinity of the earthquake epicenter in the bays of Petit Goâve and Grand Goâve along the northern coast of the Southern Peninsula, where the tsunami was triggered by slope failures of river deltas (Hornbach et al., 2010; Fritz et al., 2013). Thirty to fifty km to the north across the Bay of Gonâve, eyewitnesses reported drawdown near the locality of Luly, well explained by the reverse component of the coseismic ground motion (Hornbach et al., 2010).

40 However, observations of run-up heights up to two meters along the southern coast of Haiti, at distances up to 100 km from the epicenter, as well as tide gauge and DART buoy records at distances of 300 km and 600 km from the epicenter, respectively, have not yet received a satisfactory explanation. Fritz et al. (2013), using the early source model from the National Earthquake Information Center (NEIC), were able to roughly match these observations by scaling coseismic slip by a factor of 4 while keeping a constant seismic moment, hence downscaling the regional rigidity coefficient. A similar *ad hoc* procedure was also
45 proposed by Newman et al. (2011) for the 2010 Mentawai, Indonesia, earthquake in order to account for the discrepancy between coseismic slip inverted from teleseismic waves and actual slip derived from geodetic measurements. This artificially lowered rigidity can indeed account for slow ruptures at subductions – "tsunami earthquakes" (Kanamori, 1972) – such as in Mentawai in 2010 or in Java in 2006 (Hébert et al., 2012), but the Haiti earthquake did not exhibit such a slow thrust rupture. Here we revisit this issue by (1) testing most of the finite-source models proposed for the 2010 Haiti earthquake, (2)
50 investigating the role that an earthquake-triggered landslide off the southern coast of Haiti may have played in tsunami generation. We show that this latter hypothesis is very likely, in line with the growing set of evidence linking tsunamis along strike-slip faults to submarine landslides (e.g., Ma et al., 1991; Yalçıner et al., 2002; Rodriguez et al., 2017).

2 Tsunami Calculation Method

The numerical method involves modeling of the initiation, propagation, and run-up of the tsunami waves. For the earthquake
55 source, we calculate the initial seafloor perturbation – assumed to be instantaneously and fully transmitted to the water column – using coseismic static ground displacement for a dislocation in an elastic half-space (Okada, 1992). For the landslide source, we assumed that the sediment collapse obeys a viscous flow, consistent with the mud or shale nature of the sediments involved (Assier-Rzadkiewicz et al., 2000). We keep the dynamic viscosity constant during the whole simulation, which may not be realistic in terms of landslide propagation but has little effect on the free surface, which is mostly sensitive to the initial
60 landslide acceleration (e.g., Løvholt et al, 2015; Poupardin et al., 2017).

The tsunami propagation calculation accounts for dispersive terms in the deep ocean (Boussinesq equations) and neglects them near the coast (St Venant equations), retaining only the lowest-order nonlinear terms. In the latter case, we use a shock-capturing method to propagate strong nonlinear waves. In the former one, we use an iterative Crank-Nicholson method to solve the Boussinesq equations (details in Poupardin et al., 2017). Propagation equations are solved using a finite-difference scheme

65   with a spatial discretization that uses centered differences for linear terms and forward differences for advection terms (Hébert
      et al., 2001).

      We solve the numerical problem using four successive levels of nested bathymetric grids from the deep ocean to the local
      coastal areas of interest. The two lower resolution grids use the GEBCO World Bathymetry with a resolution from 1600 to
      400 m. We digitized local bathymetric charts and included existing digital bathymetric data in the bays of Port-au-Prince,

70   Jacmel, and Santo-Domingo to build local grids with a resolution of 25 m in order to accurately model near-shore resonance
      and amplification. We used the 1600 m resolution grid to propagate the tsunami to the DART Buoy and the 25 m one for the
      Santo Domingo tide gauge in order to account for resonance due to coastal bathymetry.

3 Earthquake-generated tsunami

      We tested a uniform slip of 1 m using the NEIC fault geometry and rupture mechanism, as in Fritz et al. (2013; hereafter

75   denoted the F model), as well as 4 finite-source models with variable coseismic slip derived from combinations of GPS, InSAR,
      coastal uplift, and teleseismic data (Hayes et al., 2010; Meng et al., 2012; Symithe et al., 2013; Saint Fleur et al., 2015; hereafter
      denoted the H, M, S, and SF models, respectively). All finite-source models show that rupture occurred on a north-dipping
      blind fault (Leogâne fault) with 2/3 of the moment released by strike-slip motion and 1/3 by reverse motion, consistent with
      up to 60 cm of coastal uplift observed in the epicentral area (Hayes et al., 2010). The NEIC source model, based on teleseismic

80   data only, shows the same coseismic motion partitioning, but on a south-dipping fault with a north-verging reverse component.
      Static coseismic displacements from the finite-source models show up to 0.5-1 m of seafloor uplift north of the rupture (Fig.
      2) and less than 0.01 m of subsidence along the southern coastline. The F model shows an opposite pattern because of its fault
      dip opposite to the finite-source models, and larger coseismic displacement because of the *ad hoc* coseismic slip scaling factor
      applied (see above). This model is inconsistent with the coseismic geodetic observations and the coseismic coastal uplift

85   observed in the epicentral area. It matches observations at the Santo Domingo tide gauge and DART buoy 42407 reasonably
      well in amplitude and period at low frequencies, but its coseismic slip was arbitrarily tuned to match these observations (Fig.
      3).

      All finite-source models predict a small tsunami in the epicentral area, with the M and SF models predicting wave heights of
      up to 1 m along more than 10 km of coastline length, inconsistent with the observations reported by the ITST team (Fritz et

90   al., 2013). Indeed, coseismic coastal uplift in the M and SF models are larger and more spread out than the observations
      reported in Hayes et al. (2010). All finite-source models predict a local tsunami at Luly, with 0.5-1 m run-up height (Fig. 2),
      consistent with observations at that location (Hornbach et al., 2010). This local tsunami likely occurred as a result of the
      intersection of the coastline with the sharp edge of the bathymetric low that occupies most of the Bay of Port-au-Prince. Only
      the F model predicts significant wave heights along the southern coast (Fig. 4), but it also predicts run-up heights of 0.5-1 m

95   in the highly populated and low-lying coastal region surrounding the capital city of Port-au-Prince that were not observed after
      the earthquake (Fig. 2).

That none of the finite-source models comes close to the observations in the near field in Jacmel and Pedernales or in the far field at two locations 450 km apart likely indicates the presence of a secondary tsunami source. An offshore landslide comes to mind, as they are well known to trigger tsunamis even at large distances (e.g., Heinrich et al., 2001; Okal and Synolakis, 2004; Fritz et al., 2007; Hébert et al., 2012). Fritz el al. (2013) indeed already suspected that this type of source may be required to explain field observations near Jacmel and Pedernales.

4 Landslide-generated tsunami

We used a high-resolution bathymetry recently acquired offshore the southern coast of Hispaniola (Leroy et al., 2015) to search for scars in the seafloor morphology that could be indicative of large submarine landslides within the area significantly shaken by the earthquake. The fact that the earthquake source approximately matches observed arrival times at the tide gauge and DART buoy is an indication that a possible landslide source should be located fairly close to the epicentral area, which is a requirement for seafloor acceleration to be sufficient to trigger slope failure.

We found the clearest and largest landslide signature 30 km due south of the tip of the cape that bounds the bay of Jacmel to the west, at a water depth of 3500 m (Fig. 5). The landslide is expressed on the seafloor by two arcuate scars at the slope break between a flat plateau (Haiti Plateau) marked by a sediment wave field and a narrow canyon likely feeding the northeastern corner of the 5000 m-deep Haiti sub-basin (Mauffret and Leroy, 1999). The scar shows two horseshoe-shaped lobes with sharp edges, opening to the east onto the narrow canyon that likely acted as an evacuation pathway for the sediments. Unfortunately, no chirp or high-resolution seismic data is available crossing that feature, which has not been cored either, so that one cannot determine the age of the sediment collapse.

We tested that landslide as the plausible secondary source necessary to explain the observations in the near field (southern coastline) and far field (tide gauge and DART buoy) of the earthquake. We used the detailed bathymetry (Fig. 5) to reconstruct the sedimentary volume involved in the landslide, as in ten Brink et al. (2006). It consists in filling-in the failed area according to the adjacent scar height, to reconstruct the seafloor morphology prior to the slide. By using this method, we find a volume of 2 km^3, a maximum thickness of 150 m, and a slope of 10°. Once triggered, the failed volume flows with maximum velocities in the 10–65 m/s range depending on the assumed viscosity (Fig. 6). The initial acceleration remains approximately the same at ~0.5 m/s² for all tested dynamic viscosities but it quickly decreases for the dynamic viscosity of 2×10^5 Pa.s, resulting in smaller amplitudes within the model domain. The influence of the viscosity is evaluated by considering water heights calculated at a synthetic gauge located offshore, a few kilometer north of the landslide (gauge G_1 in Fig. 8). As expected, the larger the viscosity, the smaller the amplitudes of water waves, whereas periods are unchanged (Fig. 7). The largest viscosity results in maximum wave amplitudes below 50 cm at the location of gauge G_1.

In our preferred model, the southern coast of the Dominican Republic is reached by water waves within 5 to 10 minutes of the landslide triggering. Maximum water heights after one hour of propagation (Fig. 8) show that water waves are amplified along an arc segment extending from the landslide area towards the Bay of Jacmel. The maximum wave heights reach 2 to 3 m along a coastal segment of 10 km for a viscosity of 2×10^5 Pa.s (Fig. 8) consistent with ITST observations (Fritz et al., 2013).

130   Model results at synthetic gauge G_2 located in the bay of Jacmel show that maximum wave amplitudes range from 3 to 6
meters depending on the viscosity of the sliding material (Fig. 9). ITST measurements at Jacmel (see Fig. 5c in Fritz et al.,
2013), around 3 m, favor a sliding material with a viscosity in the high range of the ones tested here. Due to the local
amplification of the bay, the maximum water height at Jacmel occurs 11 minutes after the underwater slope failure consistent
with observations.

135   Further along the coast, the comparison of calculated and observed time series at the Santo Domingo tide gauge is shown in
Fig. 10. Data are available with a 1-minute sampling rate and the tide gauge is located at the end of a small harbor that is poorly
described in the simulation. Nevertheless, the arrival time of the first wave (about 45 min) as well as the periods and amplitudes
of water waves are approximately reproduced by the model.

In the offshore direction, wave propagation is subject to frequency dispersion, which the model takes into account by solving
140   Boussinesq equations. In Fig. 10, we compare the calculated time series at synthetic gauge G_1 with recorded data at DART
Buoy 42407 with a sampling rate of 1 min. Due to frequency dispersion, the highest water height in the calculated wave train
is not the first one but the third, with an amplitude of 0.5 cm. The arrival times as well as amplitudes of the first two waves
match the observed signal well. Nevertheless, the oscillations of the following waves (around 3 min) have periods that are
shorter than the observed ones (around 4 minutes), which could indicate that the simulated landslide volume is insufficient to
145   explain the observations.

5 Discussion

We first ask whether ground acceleration during the 2010 Haiti earthquake would be sufficient to trigger slope failure at the
location of the earthquake described above. We estimate the resonance frequency of the landslide using $f = V_s/4H$ where V_s
is the shear-wave velocity and H the landslide thickness (Parolai et al., 2002). For $V_s = 1000$ m/s and $H = 100$ m f is 2.5 Hz,
150   a high-enough frequency to justify using PGA as a proxy for the acceleration that determines slope failure. It is generally
recognized that 0.1–0.2 g PGA is the threshold of stability for the triggering of landslides in benthic sediments (e.g., Keefer,
1984, Meunier et al., 2007). Tanyaş et al. (2017) show that 80% of earthquake-induced on-land landslides are observed in the
PGA interval 0.1-0.8 g. Offshore, sedimentation rates, the state of sediment consolidation, and the occurrence of weak layers
determine the potential of seismic shaking to increase pore pressure up to the failure threshold. As a result, large PGA does
155   not always trigger mass flow, whereas low PGA can sometimes be sufficient (Hampton et al., 1996; Viesca and Rice, 2012;
ten Brink et al., 2016; Pope et al., 2017). For example, the study of Janin et al. (2019) on holocene sediment collapses along
the North Anatolian Fault in the Marmara Sea, shows that water circulation induced by seismic shaking in the material can
have a significant effect on landslide triggering.

There was no direct measurement of regional ground acceleration during the 2010 Haiti earthquake, but indirect estimates
160   from rigid body displacements and structural damage infer a PGA value of 0.2-0.4 g in Port-au-Prince (Olson et al., 2011;
Goodno et al., 2011; Hough et al., 2012), ~30 km east of the earthquake epicenter. A numerical ground motion study based on
the coseismic slip distribution from Hayes et al. (2010) finds the mean PGA in Port-au-Prince to be 0.20-0.33g (Mavroeidis

and Scotti, 2013). We computed a first-order estimate of the horizontal ground acceleration at the location of the offshore landslide described above using the "Next Generation Attenuation Ground Motions code" (Boore, 2012) for a M7 earthquake

165   (Fig. 11). We find PGA values on the order of 0.1 g at a distance of 30 km to the earthquake epicenter on soft rock (shear wave velocity near surface Vs30 of 530 m/s). We also used the more precise, but more complex, approach based on a dynamic rupture simulation of the 2010 earthquake on a fault of realistic geometry, as described in Douilly et al. (2015, 2017). Using the same source as these authors, which satisfies observations of static coseismic ground displacement, we find the largest horizontal peak ground acceleration at 0.18 g, for the E-W component while the mean horizontal peak ground acceleration is

170   0.17 g (Fig. 11). These two ground motion estimates are consistent with each other, though one must keep in mind that these calculations do not account for the more complex near-surface sediment structure likely to be present in the area of the submarine landslide.

Although there is no direct evidence that the submarine landslide described above was triggered by the 2010 Haiti earthquake, it appears that seafloor acceleration in that area was within the range that permits slope failure in marine sediments. It is

175   therefore plausible that a submarine landslide off the southern coast of Haiti is the secondary source necessary to explain, at the same time, the far-field tide gauge and DART buoy observations and the exceptionally large run-up heights at a few locations along the southern coast of Haiti given the limited coseismic displacement there.

A number of similar examples have been documented, often in subduction contexts. For instance, the 1998, M_w7.0, Papua New Guinea earthquake was followed by a tsunami with run-up heights of over 7 m on a 20 km-long coastal segment, too

180   large to be accounted for by the coseismic ground displacement alone (Okal and Synolakis, 2001; Tappin et al., 2008). Numerical simulations showed that the tsunami could be attributed to a submarine landslide with a volume of 4 km^3 located 20 km offshore (Heinrich et al., 2001). Similarly, the 2006 Java tsunami produced run-up heights up to 20 m at Permisan, indicative of a submarine landslide off the Nusa Kambangan Island (Fritz et al., 2007, Hébert et al., 2012). In the northern Caribbean, López-Venegas et al. (2008) argue that the tsunami associated to the October 11, 1918 M7.5 normal faulting

185   earthquake in the Mona Passage between Hispaniola and Puerto Rico was the result of a submarine landslide at a ~2000 m depth. Run-up heights in western Puerto Rico reached up to 6 m about 20 km from the landslide, whose volume was estimated at 10 km^3, 5 times that of the landslide described here. In a tectonic context similar to the 2010 Haiti earthquake, the 1989, M_w6.9, Loma Prieta earthquake excited tsunamis in the nearby Monterey Bay that required a secondary offshore landslide, assumed to have occurred in shallow waters (Ma et al., 1991).

190   In northern Haiti, the M7.6 to 8.0, 1842 May 7 earthquake was followed by a tsunami that killed ~300 people, with wave heights of 2 m reported at a few locations along the northeastern Haitian coast and a maximum run-up of 4.6 m in the city of Port-de-Paix (Scherer, 1912). Some far-field effects have been reported, but their reliability remains questionable (O'Loughlin and Lander, 2003). Because it is the fastest-slipping active fault closest to the affected area, the Septentrional Fault is commonly assumed to be the source of that earthquake. However, a recent study shows that an 1842-like strike-slip earthquake

195   on that fault cannot explain the tsunami run-up heights observed (Gailler et al., 2015). As a consequence, these authors suggest that event may have occurred on the North Hispaniola Fault, a slow-slipping reverse faults ~50 km offshore. The MMI IX

intensities estimated along the Northern Haiti coastline for the 1842 earthquake suggest accelerations on the order of 0.3 g (Murphy and O'Brien 1977). It is therefore plausible that a strike-slip event on the Septentrional Fault would have triggered submarine slope failures – possibly multiple ones – along the steep and near-shore slopes that characterize the bathymetry of
200   the northern Haiti margin (Leroy et al., 2015).

6 Conclusion

Underwater mass movements have been suggested for more than 100 years to trigger tsunamis in the near field of large earthquakes (e.g., Verbeek 1900; Gutenberg 1939). They are now considered to be significant contributors to tsunami hazard (e.g. Synolakis et al. 2002; ten Brink et al., 2006; Okal et al. 2009). It has been noted that tsunamis in strike-slip tectonic
205   regimes were more frequent than expected (e.g., Ma et al., 1991; Yalçıner et al., 2002; Hornbach et al., 2010). That local earthquakes can trigger shallow submarine slope failures is well known and was documented following the 2010 Haiti earthquake, in its epicentral area (Hornbach et al., 2010; Fritz et al., 2013). Here we show that deep submarine landslides can also produce significant tsunamis in this area, as also proposed for Puerto Rico (López-Venegas et al., 2008). This result contributes to explaining why many tsunamis occur along strike-slip fault systems, especially when steep submarine slopes
210   are within reach of significant coseismic ground acceleration, as is the case along most strike-slip fault systems in the Caribbean.

Acknowledgements

This work was funded by the "Yves Rocard" Joint Laboratory between the Ecole normale supérieure, the Commissariat à l'Energie Atomique, and the CNRS. The authors thank colleagues from the Institut de Physique du Globe for sharing their
215   source model for the 2010 Haiti earthquake.

References

Abrahamson, N. and Silva, W.: Summary of the Abrahamson& Silva NGA Ground motion relations, Earthq. Spectra, 24, 67-97, 2008.

Assier-Rzadkiewicz, S., Heinrich, P., Sabatier, P., Savoye, B., Bourillet, J. F.: Numerical modelling of a landslide-generated
220   tsunami: the 1979 Nice event, Pure Appl. Geophys., 157, 1707–1727, 2000.

Boore, D. M. and Atkinson, G. M.: Ground-motion prediction equations for the averaged horizontal component of PGA, PGV, and 5%-damped PSA at spectral periods between 0.01s and 10.0s, Earthq. Spectra, 24, 99-138, 2008.

Boore, D. M.: NGA08_GM_TMR, Next generation attenuation ground motions for specified period (T), magnitude, and distance (R) code, revised version, www.daveboore.com, 2012.

225   Calais, E., Freed, A., Mattioli, G., Amelung, F., Jonsson, S., Jansma, P., Hong, S. H., Dixon, T., Prepetit, C., Momplaisir, R.: Transpressional rupture of an unmapped fault during the 2010 Haiti earthquake, Nature Geoscience, 3(11), 794–799, 2010.

Campbell, K. W. and Bozorgnia, Y.: NGA Ground motion model for the geometric mean horizontal component of PGA, PGV, PGD and 5% damped linear elastic response spectra for periods ranging from 0.01 to 10 s, Earthq. Spectra, 24, 139-171, 2008.

Chiou, B. S.-J. and Youngs, R. R.: An NGA model for the average horizontal component of peak ground motion and response spectra, Earthq. Spectra, 24, 173-215, 2008.

Dietz L. D., and Ellsworth, W. L.: The October 17, 1989, Loma Prieta, California, Earthquake and its aftershocks: Geometry of the sequence from high-resolution locations, Geophys. Res. Lett., 17(9), 1417–1420, 1990.

Douilly, R., Aochi, H., Calais, E., and Freed, A.: Three-dimensional dynamic rupture simulations across interacting faults: The M_w7.0, 2010, Haiti earthquake. J. Geophys. Res. Solid Earth 120, 1108–1128, 2015.

Douilly, R., Mavroeidis, G. P., and Calais, E.: Simulation of broadband strong ground motion for a hypothetical M_w7.1 earthquake on the Enriquillo Fault in Haiti, Geophys. J. Int., 211, 400-417, 2017.

Fritz, H. M., Kongko, W., Moore, A., Macadoo, B. G., Goff, J., Harbitz, C., Uslu, B., Kalligeris, N., Suteja, D., Kalsum, K., Titov, V., Gusman, A., Latief, H., Santoso, E., Sujoko, S., Djulkarnaen, D., Sunendar, H. and Synolakis, C.: Extreme runup from the 17 July 2006 Java tsunami, Geophys. Res. Letter, 34, L12602, 2007.

Fritz, H. M., Hillaire, J. V., Molière, E., Wei, Y. and Moham-med, F.: Twin tsunamis triggered by the 12 January 2010 Haiti earthquake, Pure Appl. Geophys., 170, 1463-1474, 2013.

Gailler, A., Calais, E., Hébert, H., Roy, C., and Okal, E.: Tsunami scenarios and hazard assessment along the northern coast of Haiti, Geophysical Journal International, 203(3), 2287–2302, 2015.

Goodno, B., Gould, N., Caldwell, P., and Gould, P.: Effects of the January 2010 Haitian earthquake on selected electrical equipment. Earthquake Spectra, 27, S251–S276, 2011.

Gutenberg, B.: Tsunamis and earthquakes, Bull. seism. Soc. Am., 29, 517–526, 1939.

Hampton, M. A., Locat, J., and Lee, H. J.: Submarine landslides, Reviews of Geophysics, 34(1), 33–59, 1996.

Hashimoto, M., Fukushima Y., and Fukahata, Y.: Fan-delta uplift and mountain subsidence during the Haiti 2010 earthquake, Nature Geoscience, 4(4), 1–5, 2011.

Hayes, G. P., Briggs, R. W., Sladen, A., Fielding, E. J., Prentice, C., Hudnut, K., Mann, P., Taylor, F. W., Crone, A. J., Gold, R., Ito, T. and Simons M.: Complex rupture during the 12 January 2010 Haiti earthquake, Nature Geoscience, 3, 800-805, 2010.

Hébert, H., Heinrich, P., Schindelé, F., and Piatanesi, A.: Far-field simulation of tsunami propagation in the Pacific Ocean: impact on the Marquesas Islands (French Polynesia), J. Geophys. Res., 106(C5), 9161–9177, 2001.

Hébert, H., Burg, P. E., Binet, R., Lavigne, F., Allgeyer, S., and Schindelé, F.: The 2006 July 17 Java (Indonesia) tsunami from satellite imagery and numerical modelling: a single or complex source? Geophys. J. Int., 191(3), 1255–1271, 2012.

Heinrich, P., Piatanesi, A., Hébert, H.: Numerical modeling of tsunami generation and propagation from submarine slumps: the 1998 Papua New Guinea event, Geophys. J. Int., 145(1), 97-111, 2001.

Hornbach, M. J., Braudy, N., Briggs, R. W., Cormier, M.- H., Davis, M; B., Diebold, J. B., Dieudonne, N., Douilly, R., Frohlich, C., Gulick, S. P. S., Johnson, H. E., Mann, P., McHugh, C., Ryan-Mishkin, K., Prentice, C. S., Seeber, L., Sorlien, C. C., Steckler, M. S., Symithe, S. J., Taylor, F. W., and Templeton, J.: High tsunami frequency as a result of combined strike-slip faulting and coastal landslides, Nature Geosciences 3, 783-788, 2010.

Hough, S. E., Taniguchi, T., and Altidor, J. R.: Estimation of peak ground acceleration from horizontal rigid body displacement: A case study in Port-au-Prince, Haiti, Bull. Seismol. Soc. Am., 102, 2704–2713, 2012.

Janin, A., Rodriguez, M., Sakellariou, D., Lykousis, V. and Gorini, C., Tsunamigenic potential of a Holocene submarine landslide along the North Anatolian Fault (northern Aegean Sea, off Thasos island): insights from numerical modelling, Nat. Hazards Earth Syst. Sci., 19, 121–136, 2019, https://doi.org/10.5194/nhess-19-121-2019, 2019.

Kanamori, H.: Mechanism of tsunami earthquakes, Physics of the Earth and Planetary Interiors, 6, 346–359, 1972.

Keefer, D. K.: Landslides caused by earthquakes, Geological Society of America Bulletin, 95, 406-421, 1984.

Leroy, S., Ellouz-Zimmermann, N., Corbeau, J., Rolandone, F., de Lépinay, B.M., Meyer, B., Momplaisir, R., Granja Bruña, J.L., Battani, A., Baurion, C., Burov, E., Clouard, V., Deschamps, R., Gorini, C., Hamon, Y., Lafosse, M., Leonel, J., Le Pourhiet, L., Llanes Estrada, P., Loget, N., Lucazeau, F., Pillot, D., Poort, J., Tankoo, K.R., Cuevas, J.L., Alcaide, J.F., Jean Poix, C., Muñoz-Martin, A., Mitton, S., Rodriguez, Y., Schmitz, J., Seeber, L., Carbo- Gorosabel, A., Muñoz, S.: Segmentation and kinematics of the North America-Caribbean plate boundary offshore Hispaniola, Terra Nova, 27(6), 467–478, 2015.

Løvholt F., Pedersen, G., Harbitz, C. B., Glimsdal, S., Kim, J.: On the characteristics of landslide tsunamis, Phil. Trans. R. Soc. A, 373(2053), 20140376, 2015.

280 López-Venegas, A.M., ten Brink, U. S., and Geist, E. L.: Submarine landslide as the source for the October 11, 1918 Mona Passage tsunami: Observations and modeling, Marine Geology, 254(1), 35-46, 2008.

Ma, K. F., Satake, K., and Kanamori, H.: The origin of the tsunami excited by the 1989 Loma Prieta earthquake faulting or slumping? Geophys. Res. Lett., 18, 637–640, 1991.

Mauffret, A., and S. Leroy: Neogene intraplate deformation of the Caribbean plate at the Beata Ridge, Sedimentary Basins of 285 the World, 4, 627–669, 1999.

Mavroeidis, G. P., and Scotti, C. M.: Finite-Fault Simulation of Broadband Strong Ground Motion from the 2010 Mw 7.0 Haiti Earthquake, Bulletin of the Seismological Society of America, 103(5), 2557–2576, 2013.

Meng, L., Ampuero, J. P., Sladen, A. and Rendon, H.: High-resolution backprojection at regional distance: Application to the Haiti M 7.0 earthquake and comparisons with finite source studies, J. Geophys. Res., 117, B04313, 2012.

290 Meunier, P., Hovius, N., Haines, A. J.: Regional patterns of earthquake-triggered landslides and their relation to ground motion, Geophysical Research Letters, Volume 34, Issue 20, https://doi.org/10.1029/2007GL031337, 2007.

Murphy, J. R., and O'Brien, L. J. The correlation of peak ground accel- eration amplitude with seismic intensity and other physical parameters, Bull. seism. Soc. Am., 67, 877–915, 1977.

Newman, A. V., Hayes, G., Wei, Y., and Convers, J.: The 25 October 2010 Mentawai tsunami earthquake from real-time 295 discriminants, finite-fault rupture, and tsunami excitation, Geophys. Res. Lett., 38, L05302, 2011.

Okada, Y.: Internal deformation due to shear and tensile faults in a half-space, Bulletin of the Seismological Society of America, 82(2), 1018–1040, 1992.

Okal, E. A. and Synolakis, C. E.: Comment on « Origin of the 17 July 1998 Papua New Guinea Tsunami: earthquake or landslide? », Seismological Research Letters, 72(3), 362–266, 2001.

300 Okal, E. A. and Synolakis, C. E.: Source discriminants for near-field tsunamis, Geophysical Journal International, 158(3), 899–912, 2004.

Okal, E. A., Synolakis, C. E., Uslu, B., Kalligeris, N., and Voukouvalas, E.: The 1956 earthquake and tsunami in Amorgos, Greece. Geophysical Journal International, 178(3), 1533-1554, 2009.

O'Loughlin, K. F., and Lander, J. F.: Caribbean Tsunamis: A 500-Year History from 1498–1998, v.20, Springer, 2003.

305 Olson, S. M., Green, R. A., Lasley, S., Martin, N., Cox, B. R., Rathje, E., Bachhuber, J., and French, J.: Documenting liquefaction and lateral spreading triggered by the 12 January 2010 Haiti earthquake, Earthquake Spectra, 27, S93–S116, 2011.

Papageorgiou, A. S., Aki, K.: A specific barrier model for the quantitative description of inhomogeneous faulting and the prediction of strong ground motion. Part I. Description of the model, Bull. Seism. Soc. Am., 73, 693-722, 1983.

310 Parolai, S., Bormann, P., Milkereit, C.: New Relationships between Vs, Thickness of Sediments, and Resonance Frequency Calculated by the H/V Ratio of Seismic Noise for the Cologne Area (Germany), Bulletin of the Seismological Society of America, 92(6), 2521-2527, 2002.

Pope, E. L., Talling, P. J., and Carter L.: Which earthquakes trigger damaging submarine mass movements: Insights from a global record of submarine cable breaks? Marine Geology, 384, 131–146, 2017.

315 Poupardin, A., Heinrich, P., Frère, A., Imbert, D., Hébert, H., and Flouzat, M.: The 1979 Submarine Landslide-Generated Tsunami in Mururoa, French Polynesia, Pure and Applied Geophysics, 174(8), 3293–3311, 2017.

Rodriguez, M., Maleuvre, C., Jollivet-Castelot, M., d'Acremont, E., Rabaute, A., Lafosse, M., Ercilla, G., Vázquez, J. T., Alonso, B., Ammar, A., and Gorini, C.: Tsunamigenic submarine landslides along the Xauen-Tofiño banks in the Alboran Sea (Western Mediterranean Sea), Geophysical Journal International, 209(1), 266-281, 2017.

320 Saint Fleur, N., Feuillet, N., Grandin, R., Jacques, E., Weil-Accardo, J., and Klinger, Y.: Seismotectonics of southern Haiti: A new faulting model for the 12 January 2010 M7.0 earthquake, Geophys. Res. Lett, 42, 10,273–10,281, 2015.

Scherer, J.: Great earthquakes in the island of Haiti, Bull. seism. Soc. Am., 2(3), 161–180, 1912.

Symithe, S. J., Calais, E., Haase, J. S., Freed, A. M., and Douilly, R.: Coseismic Slip Distribution of the 2010 M7.0 Haiti Earthquake and Resulting Stress Changes on Regional Faults, Bull. Seism. Soc. America, 103, 2326-2343, 2013.

325 Symithe, S. J., Calais, E., Chabalier, J. B., Robertson, R., and Higgins M.: Current block motions and strain accumulation on active faults in the Caribbean, Journal of Geophysical Research, 120, 2015.

Synolakis, C. E., Bardet, J.- P., Borrero, J. C., Davies, H. L., Okal, E. A., Silver, E. A., Sweet, S., and Tappin, D. R.: The slump origin of the 1998 Papua New Guinea tsunami, Proc. Roy. Soc. Lond., A, 458, 763–789, 2002.

ten Brink, U. S., Geist, E. L., and Andrews, B. D.: Size distribution of submarine landslides and its implication to tsunami
330   hazard in Puerto Rico, Geophys. Res. Lett., 33(11), L11307, 2006.

ten Brink, U. S., Andrews, B. D., and Miller, N. C.: Seismicity and sedimentation rate effects on submarine slope stability, Geology, 44(7), 563–566, 2016.

Tanyaş, H., Cees, J., van Westen, K. E., Allstadt, M. A., Nowicki, J., Tolga, G., Randall, W. J., Jonathan, W. G., Hiroshi, P. S., Robert, G. S., Odin, M., Niels, H.: Presentation and Analysis of a Worldwide Database of Earthquake-Induced
335   Landslide Inventories. J. Geophys. Res.: Earth Surface, 122, 2017.

Tappin, D. R., Watts, P. and Grilli, S. T.: The Papua New Guinea tsunami of 17 July 1998: anatomy of a catastrophic event, Nat. Hazards Earth Syst. Sci., 8, 243–266, 2008.

Verbeek, R. D. M.: Kort verslag over de aarden zeebeving op Ceram, den 30sten September 1899, Natuurkundig Tijdschrift voor Nederlandsch-Indie, 60, 219–228, 1900.

340   Viesca, R. C., and Rice, J. R.: Nucleation of slip-weakening rupture instability in landslides by localized increase of pore pressure, J. Geophys. Res., 117(3), 255–21, 2012.

Yalçıner, A. C., Alpar, B., Altınok, Y., Özbay, I., and Imamura, F.: Tsunamis in the Sea of Marmara: Historical documents for the past, models for the future. Mar. Geol., 15, 445-463, 2002.
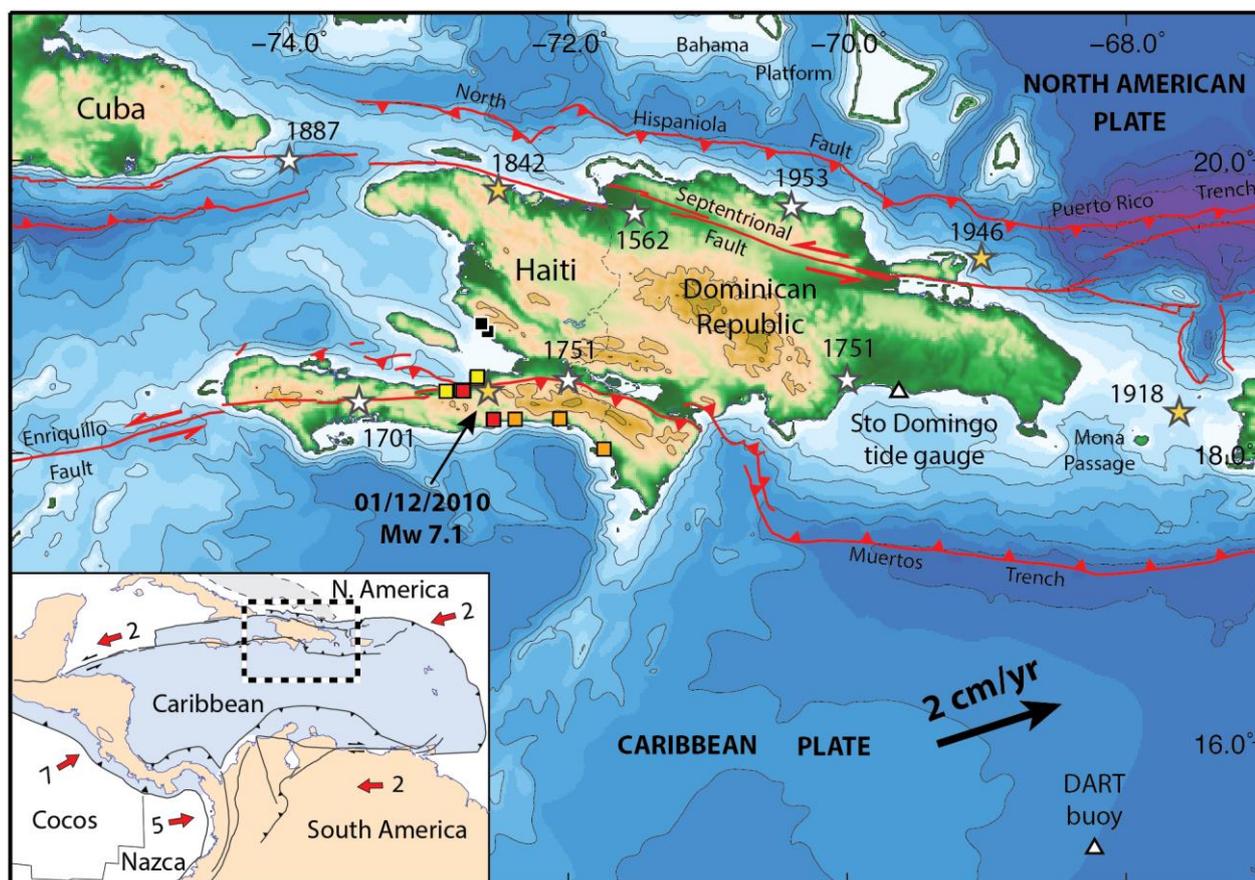
345

Figure 1: Regional tectonic context. The yellow star indicates the epicenter of the 2010, M$_w$7.0, Haiti earthquake. Other yellow stars indicate the approximate epicenter of large tsunamigenic historical earthquakes, in particular the 1842 event of northern Haiti, which is discussed in the text. White stars show the approximate location of other large historical earthquakes. Tsunami run-up heights observed after the 2010 event are indicated by squares: < 1 m (yellow), 1 to 2 m (orange), > 2 m (red), draw down (black).

350   The locations of DART buoy 42407 and Santo Domingo tide gauge are indicated by white triangles. Inset shows large-scale tectonic framework with current plate velocities relative to the Caribbean shown in cm/yr.
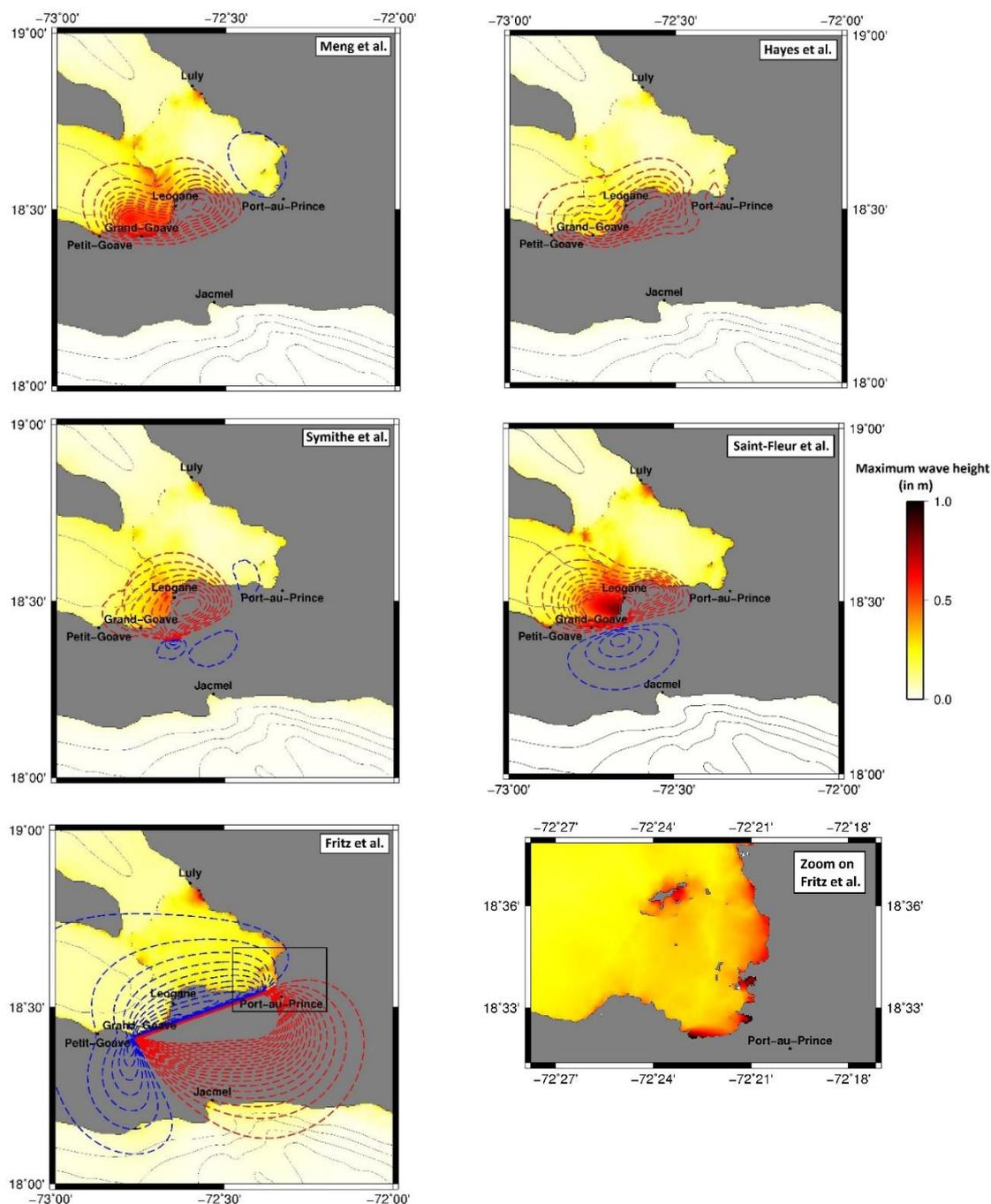
Figure 2: Initial coseismic seafloor displacement shown as dashed lines (red = uplift, blue = subsidence, contours are shown every 0.05 m) with maximum wave height shown as colored map in the background in the near field of the 2010 Haiti earthquake. H = Hayes et al., 2010, M = Meng et al., 2012, S = Symithe et al., 2013, SF = Saint Fleur et al., 2015, F =Fritz et al, 2013. Calculations are done on a 30' bathymetric grid resolution. Bottom right: blowup of the Port-au-Prince area for the F source model calculated using a 25 m resolution grid.
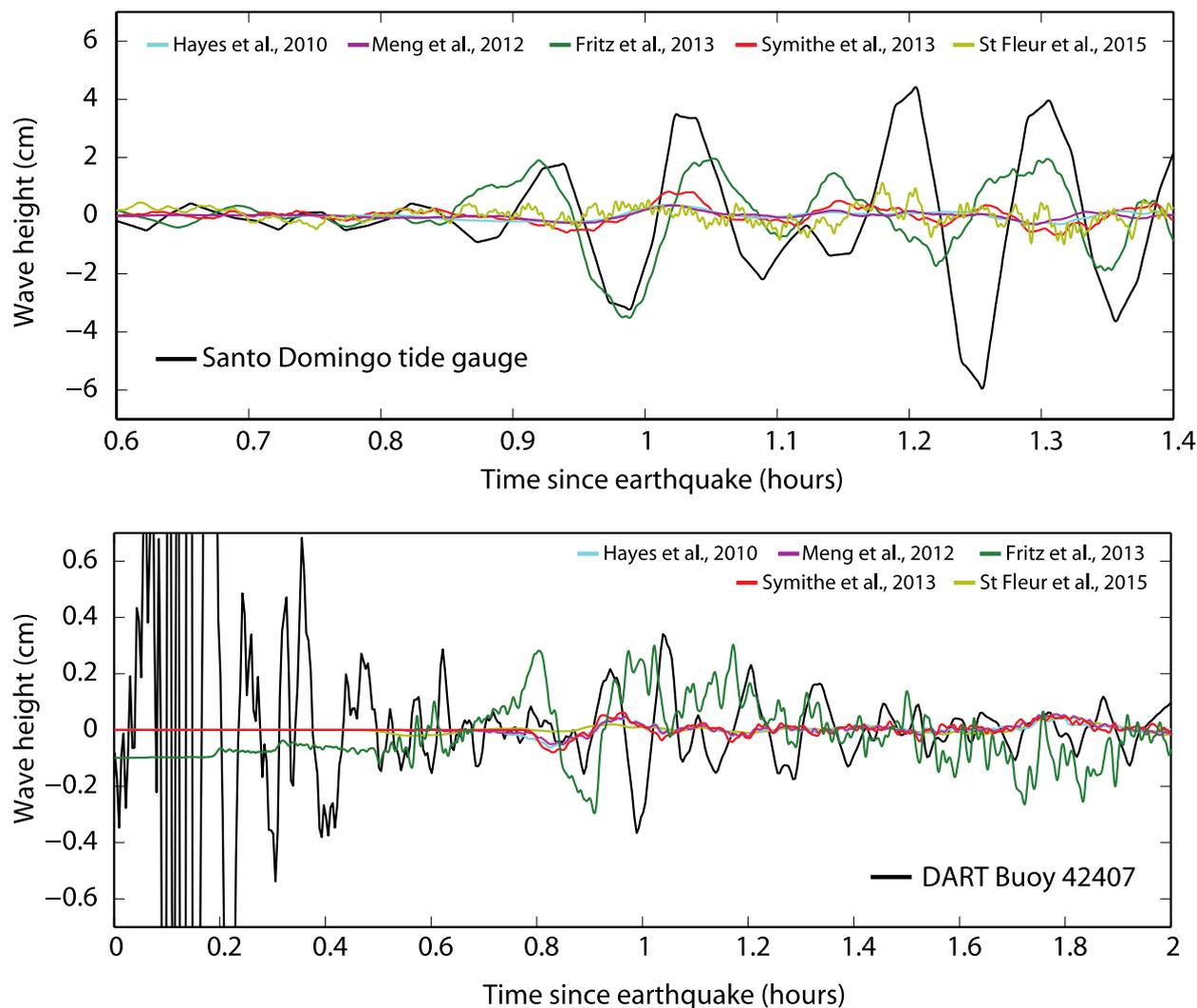
Figure 3: Comparison between observed and simulated water heights at the Santo Domingo tide gauge (top) and at DART buoy 42407 (bottom). Their locations are provided on Fig. 1. The high amplitude signal on the DART record before ~0.7 hours are seismic surface waves.
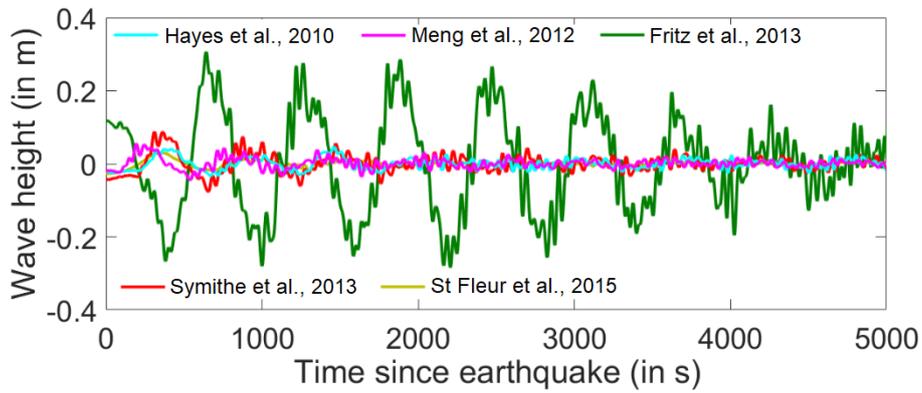
Figure 4: Water height comparison at a synthetic gauge located in the center of the Bay of Jacmel at a 30 m water depth. Calculation
365 **on a bathymetric grid uses a 30 second resolution.**
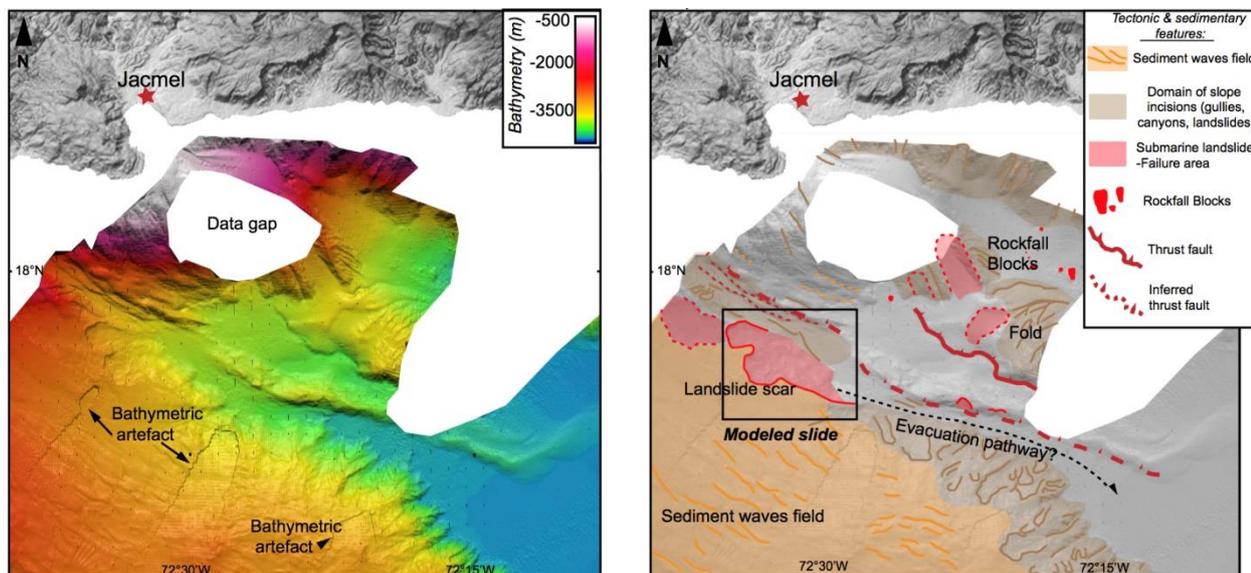
Figure 5: Detailed bathymetry 20 km due south of Jacmel (Fig. 1) where the landslide scar discussed in the text has been identified. Left: raw observations. Right: geological interpretation. Swath bathymetric data are from Haiti-sis cruise (http://dx.doi.org/10.17600/12010070).
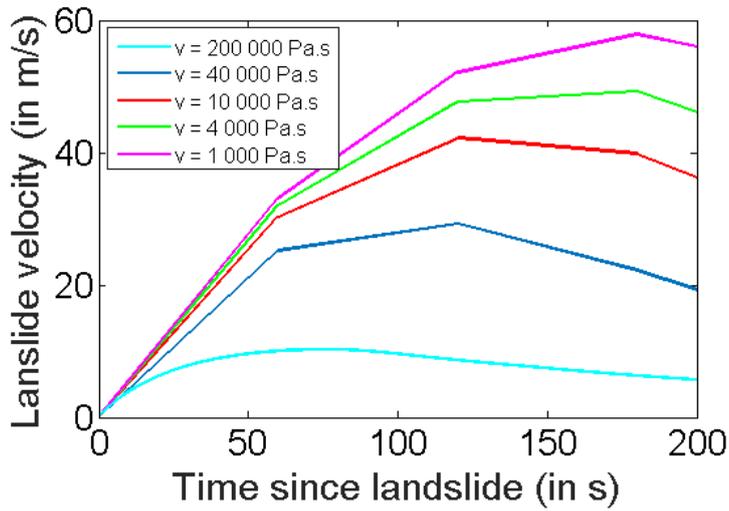
Figure 6: Landslide velocity as a function of time for the dynamic viscosities ν tested here.
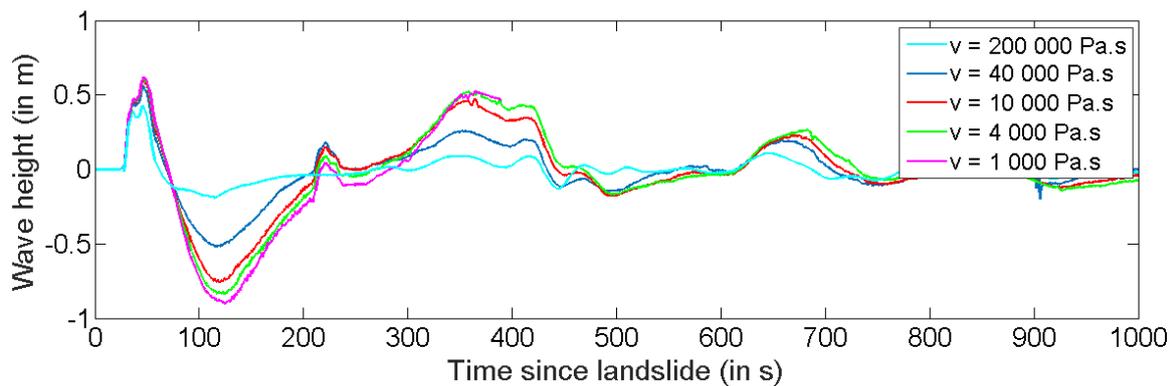
375

Figure 7: Time series calculated at the synthetic gauge G$_1$ as a function of time for the dynamic viscosities ν tested here.
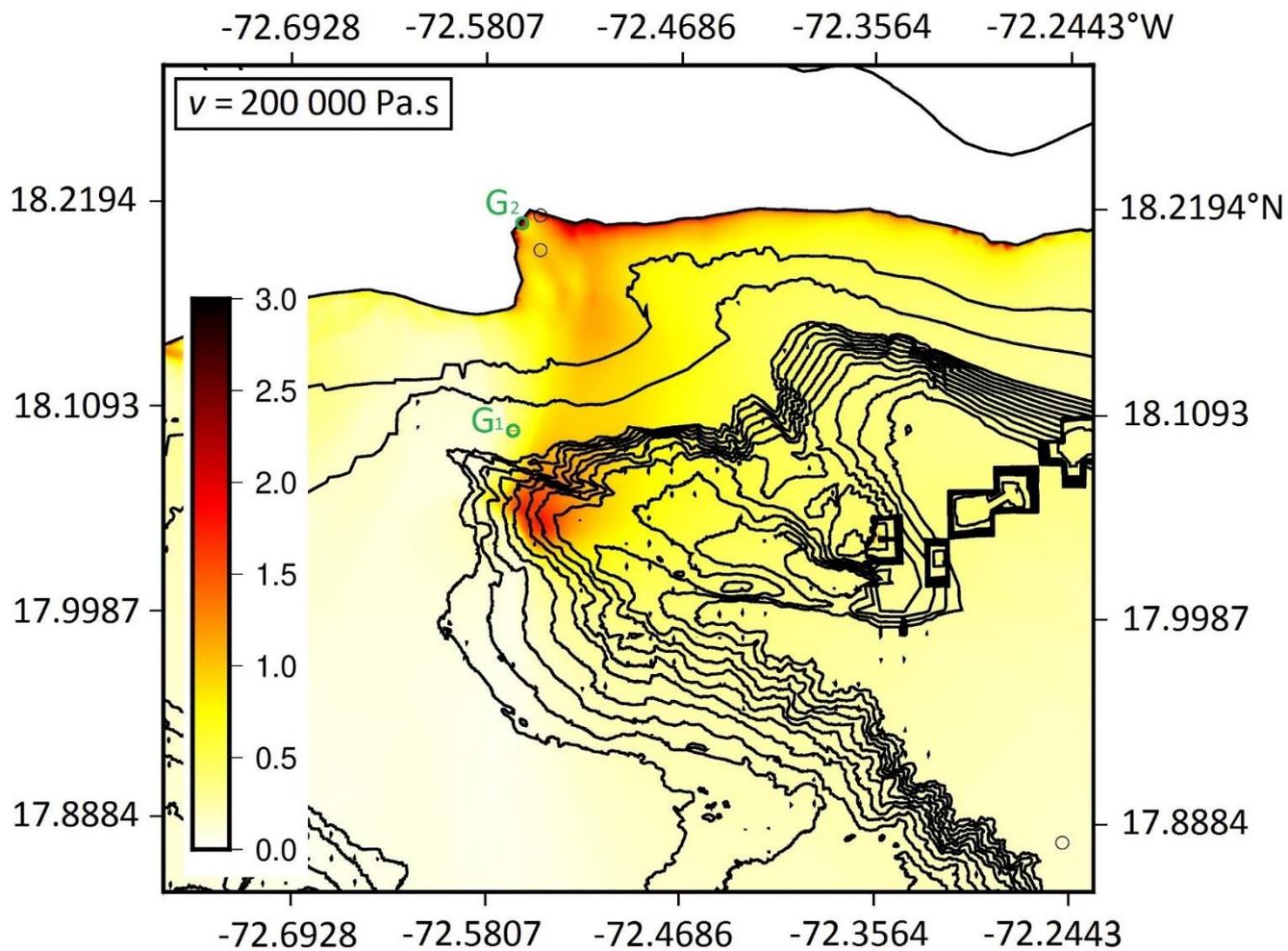
Figure 8: Maximum modeled wave height using a viscosity $v = 2 \times 10^5$ Pa.s for the sliding material.

380
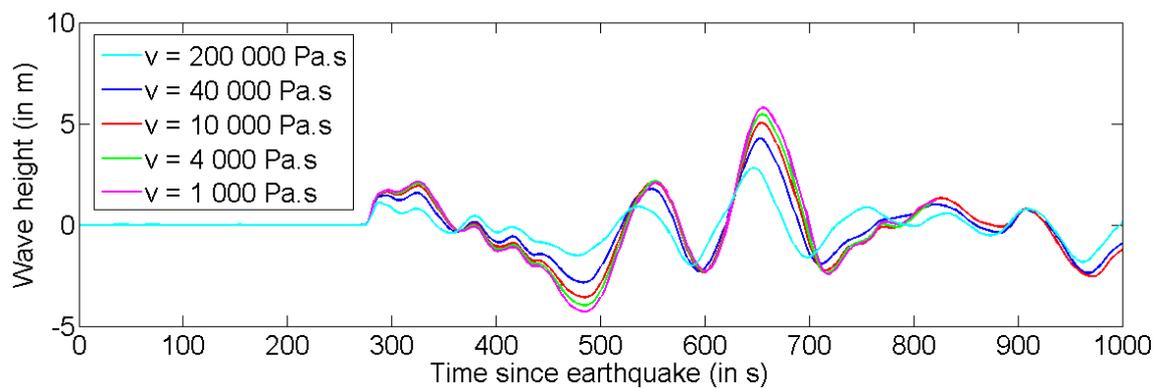
Figure 9: Time series calculated at synthetic gauge G₂ located on the coast of the Bay of Jacmel (green circle in Fig. 8). This calculation uses a bathymetric grid with 25 m resolution.
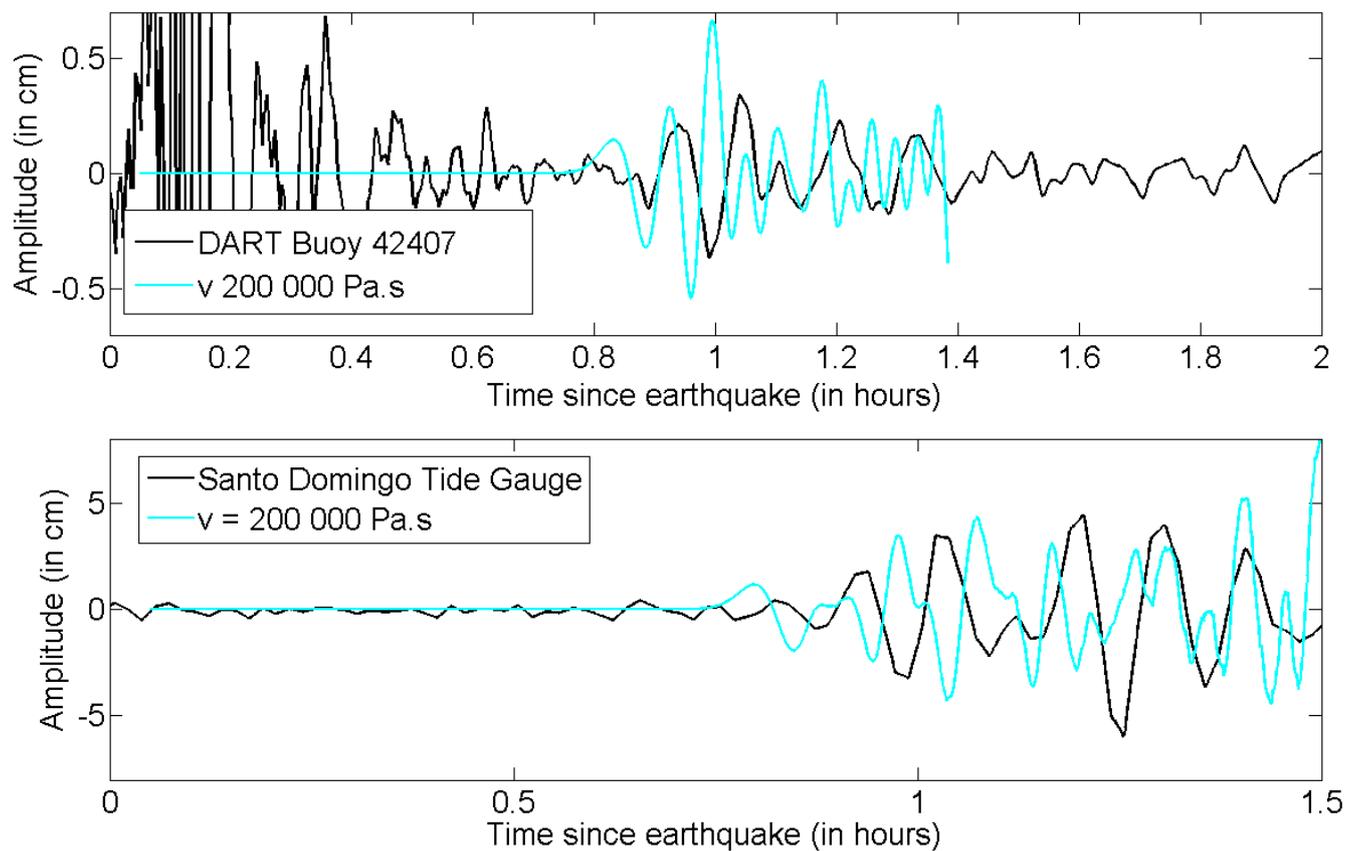
385

Figure 10: Comparison between observed and simulated water heights at the Santo Domingo tide gauge (top) and at DART buoy 42407 (bottom) for a dynamic viscosity $\nu = 2\times10^5$ Pa.s.
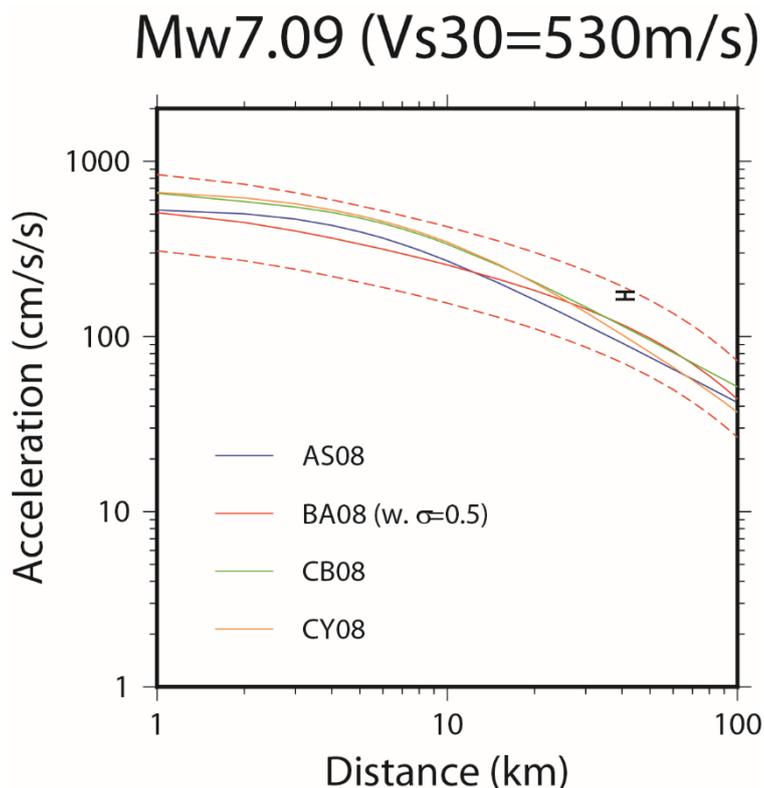
Figure 11: Estimated horizontal peak ground accelerations due to an earthquake of M$_w$7.0 from four ground motion prediction equations: Abrahamson and Silva (2008; blue line), Boore and Atkinson (2008; solid red line with ±one standard deviation in dashed lines), Campbell and Bozorgnia (2008; yellow line) and Chiou and Youngs (2008; green line). The error bar symbol shows more accurate estimates derived from hybrid broadband ground acceleration calculation at the site of interest, as proposed in Douilly et al. (2017). This combines the deterministic low-frequency part from the dynamic rupture simulation of Douilly et al. (2015) with the stochastic high frequency one calculated through the Specific Barrier Model (Papageorgiou and Aki, 1983) for a crossover frequency of 1 Hz.